Stabilizing Layered-Type K<inf>0.4</inf>V<inf>2</inf>O<inf>5</inf> Cathode by K Site Substitution with Strontium for K-Ion Batteries

ADVANCED FUNCTIONAL MATERIALS
www.afm-journal.de

Stabilizing Layered-Type $K_{0.4}V_2O_5$ Cathode by K Site Substitution with Strontium for K-Ion Batteries

*Gwangeon Oh, Shivam Kansara, Xieyu Xu, Yangyang Liu, Shizhao Xiong, and Jang-Yeon Hwang**

Developing suitable cathodes with high capacity and high power is challenging for K-ion batteries. Herein, electrochemical K-ion storage properties of the layered-type $K_{0.4}V_2O_5$ (KVO) cathode by incorporating divalent strontium ions (Sr^{2+}) into its crystal structure are enhanced. Divalent strontium ions (1.18 Å) are preferentially incorporated into the octahedrally coordinated K (1.38 Å) layers due to the similar ionic size compared to V^{4+} (0.58 Å). The introduction of 3 mmol of Sr ions in the KVO crystal improves electrical conductivity and reduces K-ion diffusion energy barriers. In addition, the strong Sr^{2+} and O^{2-} interaction acts as a structural pillar, suppressing irreversible phase transition during charge–discharge process. Multi-physics simulations clearly confirm that the $K_{0.34}Sr_{0.03}V_2O_5$ (KS3VO) cathode exhibits a more uniform K-ion distribution and enhanced reactions of K-ions compared to the KVO cathode at various depths of discharge. As a result, the KS3VO cathode demonstrates improved reversible capacity, cycling stability, and power capability over the KVO cathode in a K-ion cell. Synchrotron X-ray analysis reveals how Sr substitution enhances the electrochemical K-ion storage properties of the KS3VO cathode. In addition, the KS3VO cathode exhibits superior thermal stability and cycling stability in a full cell coupled with a hard carbon anode compared to the KVO cathode.

1. Introduction

Rechargeable K-ion batteries (KIBs), utilizing K-ion insertion materials, have garnered considerable attention for next-generation battery technology due to the attractive physicochemical properties and abundance of resources of K.[1,2] Compared to other alkali metals (Li and Na), K possesses a relatively low reduction potential (Li: −3.04 V, Na: −2.714 V, and K: −2.936 V versus the standard hydrogen electrode (SHE)), which is beneficial for achieving high-energy density.[3,4] In addition, K-ions have smaller Stokes radii in various solvents than Li- and Na- ions due to a weaker Lewis acidity, resulting in high mobility of K-ions.[5,6] Integrating these unique properties of K, KIBs can offer several benefits over Li- and Na-ion batteries.[7–9]

The energy density and durability of KIBs, akin to Li- and Na-ion batteries, depend on the reversible capacity and structural stability of the cathode materials.[10] To date, several platforms for the cathode materials have been explored, such as layered-type transition metal oxides,[11,12] polyanionic compounds,[13] and Prussian blue analogs[14] for KIBs.[15] Layered-type potassium insertion materials with a 2D structure, have emerged as high-energy and high-power cathodes due to their small molar mass and fast K-ion transport pathways.[16] However, realizing high capacity and long lifespan remains a significant challenge in the development of layered-type cathodes for K-ion batteries. This challenge arises from the hindered insertion/extraction of K-ions into/out of the structure due to their large size of 1.38 Å,[17] resulting in sluggish kinetics and suboptimal reversible capacity. Recently, layered-type potassium vanadates (i.e., $K_{0.5}V_2O_5$ and $K_2V_3O_8$) arranged with alternating K—O and V—O layers along the *c*-axis have been designed and investigated as potential cathodes for KIBs. K—O and V—O layers repeat along the *c*-axis with a substantial interlayer distance ($K_{0.5}V_2O_5$: −9.505 Å and $K_2V_3O_8$: ≈−5.3 Å), creating an ample channel for K -ion transport along the a-b plane. Based on $V^{5+/4+}$ redox reactions, layered-type $K_{0.5}V_2O_5$ can store and release K-ions into/out of its crystal structure.[18–20] Deng et al. reported that the layered-type $K_{0.5}V_2O_5$ can deliver a reversible capacity of 90 mAh g^{-1} at 10 mA g^{-1} and good cycling stability in the voltage range of 1.5–3.8 V (vs K^+ / K).[18] Later,

G. Oh, S. Kansara, J.-Y. Hwang
Department of Energy Engineering
Hanyang University
Seoul 04763, Republic of Korea
E-mail: jangyeonhw@hanyang.ac.kr
X. Xu, Y. Liu
State Key Laboratory for Mechanical Behavior of Materials
Xi'an Jiaotong University
28 Xianning West Road, Xi'an, Shaanxi 710049, China
S. Xiong
Department of Physics
Chalmers University of Technology
Göteborg SE-412 96, Sweden
J.-Y. Hwang
Department of Battery Engineering
Hanyang University
Seoul 04763, Republic of Korea
The ORCID identification number(s) for the author(s) of this article can be found under https://doi.org/10.1002/adfm.202401210

DOI: 10.1002/adfm.202401210

Li et al. synthesized a film-type $K_{0.5}V_2O_5$/CNT composite cathode (≈40 wt. % of CNTs in the composite cathode) and investigated its electrochemical K storage properties.[20] With the help of a conductive carbon, the $K_{0.5}V_2O_5$/CNT composite cathode exhibited a reversible capacity of ≈90 mAh g^{-1} at 50 mA g^{-1} in the voltage range of 1.5–3.8 V. $K_2V_3O_8$ also shows reversible K^+ storage properties with a high specific capacity of ≈100 mAh g^{-1}. Although previous studies demonstrate the reversible potassium storage properties of the layered-type potassium vanadate, intrinsic structural instability of the cathodes particularly at high working voltage region (≥3.8), showed the unsatisfactory specific capacity and cycling stability.

In this study, we introduce a potential strategy involving Sr substitution into bulk K sites to significantly enhance the structural and electrochemical properties of layered-type $K_{0.4}V_2O_5$ cathodes in KIBs, for the first time. The layered-type $K_{0.4-2x}Sr_xV_2O_5$ (x = 0, 0.03, 0.07, and 0.1) samples were successfully synthesized via the hydrothermal method. Sr^{2+} ions are incorporated into the octahedrally coordinated K^+ layers, generating vacancies at K sites and consequently enhancing K-ion diffusion kinetics. In addition, the immobile Sr in the K layer significantly suppresses irreversible phase transition during charge–discharge process due to the robust interaction between Sr^{2+} and O^{2-}. Compared to other samples, the $K_{0.34}Sr_{0.03}V_2O_5$ cathode displayed the best K^+ storage properties, including higher reversible capacity as well as better cycling stability and rate capability. Various experiments and computational simulations were performed on the electrochemical properties of the $K_{0.34}Sr_{0.03}V_2O_5$ cathode to confirm the beneficial effects of Sr substitution.

2. Result and Discussion

The series of $K_{0.4-2x}Sr_xV_2O_5$ (x = 0, 0.03, 0.07, and 0.1) samples were synthesized using a simple hydrothermal method and following a heating process. The details of the synthesis are shown in Figure S1 (Supporting information). The chemical compositions of the samples were analyzed using inductively coupled plasma-atomic emission spectroscopy (ICP-OES) (Table S1, Supporting information). Hereafter, $K_{0.4}V_2O_5$, $K_{0.34}Sr_{0.03}V_2O_5$, $K_{0.26}Sr_{0.07}V_2O_5$, and $K_{0.2}Sr_{0.1}V_2O_5$ are denoted as KVO, KS3VO, KS7VO, and KS10VO, respectively. To check the water content in the prepared materials, the thermal gravimetric analysis (TGA) was conducted for KVO, KS3VO, KS7VO, and KS10VO under N_2 atmosphere, respectively. As shown in Figure S2 (Supporting information) no weight changes were observed in TGA curves for all samples during the heating process up to 350 °C. Therefore, it is confirmed that there was no absorbed water and crystal water in the as-prepared materials.[21] Fourier-transform infrared spectroscopy (FT-IR) analysis is conducted to confirm the chemical bonding of KVO, KS3VO, KS7VO, and KS10VO. For all samples, there are no vibration absorption bands at wavenumber 2000–1200 cm^{-1}, which corresponds to the organic component incorporated with C=O, C=C, C=N, C—O, C—C, and C—N.[22] All the samples exhibit similar peaks, 998 and 762 cm^{-1}, which are attributed to the V=O stretching vibration and V—O—V vibration absorption speculated on the 998 and 762 cm^{-1}, respectively (Figure S3, Supporting information).[23] The X-ray diffraction patterns of the samples were observed using the Rietveld refinement method, and the corresponding calculated curves with refinement data are presented in **Figure 1**a,b and Figure S4a,b, and Table S2 (Supporting information). All samples are indexed by the orthorhombic phase and belong to the space group of *Cmcm*. Sr^{2+} ions are preferentially substituted for K^+ site rather than V^{4+} site, attributed to the similarity in ionic radius between Sr^{2+} (≈0.118 nm) and K^+ (≈0.138 nm), while differing from that of V^{4+} (0.058 nm). In the K layer, Sr-ions occupy the 4c Wyckoff sites, while V-ions occupy the octahedral 8f Wyckoff sites (Table S2, Supporting information). The lattice parameters of KVO, KS3VO, KS7VO, and KS10VO along the c-axis were calculated to be 18.9199, 18.9403, 18.9667, and 18.9540 Å, respectively. The refinement results show a slight elongation on the *c*-axis, as well as an increase in the intercalation layer distance, because Sr^{2+} induces the polyhedral of VO_6 to extend, and O^{2-} is attracted to the Sr^{2+} field more than the V-ion field. Nevertheless, when the substitution level of Sr^{2+} is over 0.1 mmol in K^+ sites, negligible change in the *c*-axis is observed with forming a SrV_3O_{10} impurity compound due to the solubility limit of Sr^{2+} in KVO crystal. Given the Rietveld refinement data, we can assume that the vacancy generated into the K site is due to the Sr substitution. To reveal the existence of vacancies in the KS3VO, the X-ray photoelectron spectroscopy (XPS) analysis was conducted to confirm the presence of Sr as well as the valence state of vanadium in KS3VO. No peak was observed in Sr3d spectra for KVO. In contrast, the two peaks at 134.1 and 132.3 eV correspond to the binding energies of $Sr3d_{3/2}$ and $Sr3d_{5/2}$, respectively, implying that Sr^{2+} ions are successfully substituted into the K site for KS3VO (Figure S5, Supporting information). From the V2p spectra, on the one hand, KVO and KS3VO show the similar intensity of the vanadium oxidation states of V^{4+} (516.9/517.7) and V^{5+} (524.3/525 eV). XPS results indicated that Sr substituted only into the K site and replaced K^+ with generating vacancies in the K layers. To obtain further insight existence of vacancies in the KS3VO materials, we conducted vacancy formation energy calculation and the charge density isosurfaces calculations (Figures S6 and S7, Supporting information).

Scanning electron microscope (SEM) images in Figure S8 (Supporting information) depict rod-shaped nanoparticles with average diameters of ≈100 nm, irrespective of the chemical composition. To check the surface area of the samples, we conducted Brunauer–Emmett–Teller (BET) method (Figure S9, Supporting information). The isotherms of all samples showed a similar volume adsorption value at a relative pressure of 0.01–0.6, resulting in almost identical specific surface area values (Table S3, Supporting information). SEM and BET analysis results show that the substitution of Sr at the K site does not affect the changes in particle size, shape, and surface area of the samples. The crystal structures of KVO and KS3VO were further investigated using bright-field and high-resolution transmission electron microscopy (HRTEM) (Figure 1d,g). TEM energy dispersive X-ray (EDX) mapping data showed uniform elemental distributions for KS3VO (Figure 1c), KVO, KS7VO, and KS10VO (Figure S10, Supporting information). The selected area electron diffraction (SAED) patterns of both KVO (Figure 1f) and KS3VO (Figure 1i) through the [010] zone axis showed (002) and (200) spots corresponding to the orthorhombic structure belonging to the *Cmcm* space group. In Figure 1e,h, the interplanar distances of 0.946 and 0.947 nm correspond to the (002) crystal planes of KVO and

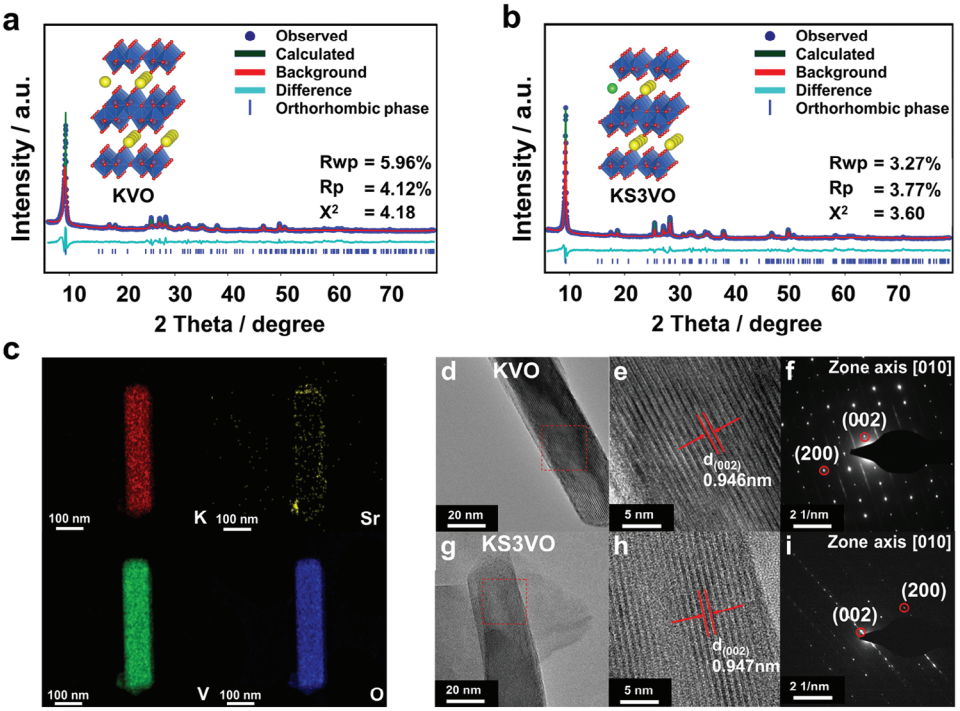

Figure 1. Rietveld refinement of X-ray diffraction (XRD) data for a) $K_{0.4}V_2O_5$ and b) $K_{0.34}Sr_{0.03}V_2O_5$ (KS3VO). c) Elemental mapping of KS3VO. d,e) HR-TEM image, and f) Selected area electron diffraction (SAED) pattern of KVO. g,h) HR-TEM image, and i) SAED pattern of KS3VO.

KS3VO, respectively. The slight enlargement in the interplanar distances of the (002) plane of KS3VO is attributed to the incensement of O^{2-}–O^{2-} repulsion by Sr substitution into the K layer, which shows a good trend with the Rietveld refinement data. To further verify the repulsion between O^{2-} and O^{2-}, we investigated the crystal structure of KS3VO in detail (Figure S11, Supporting information). Substitution of a Sr atom, leading to steric effects, into the KVO layered structure, induces notable changes in the material's interlayer distance. This alteration can be attributed to multiple factors, including the change that occurs due to the repulsion between the O^{2-} ions, induced by the presence of the Sr substitution within the K layer. As a result, the optimized structure with Sr substitution exhibits an expansion in the interlayer spacing, reflecting the repulsive interactions between the oxygen ions in adjacent layers.

To validate the preferential substitution of Sr^{2+} into the K^+ site, density functional theory (DFT) calculations were conducted, and compare the energies of K and V sites in the layered potassium vanadate crystals after Sr^{2+} substitution. Initial focus was on the theoretical formation energies of structure configurations depending on different Sr substitution level: $K_{0.375}Sr_{0.125}V_2O_5$ ($K_{0.5}Sr_{0.125}V_{1.875}O_5$), $K_{0.33}Sr_{0.083}V_2O_5$ ($K_{0.42}Sr_{0.083}V_{1.917}O_5$), $K_{0.375}Sr_{0.062}V_2O_5$ ($K_{0.44}Sr_{0.062}V_{1.937}O_5$) and $K_{0.34}Sr_{0.03}V_2O_5$ ($K_{0.34}Sr_{0.03}V_{1.969}O_5$), corresponding to models 1, 2, 3, and 4 in **Figure** 2a, respectively. A detailed description of the structural parameters is presented in Table S4 (Supporting information). As shown in Figure 2b, Sr-substituted $K_{0.4}V_2O_5$ is always more stable when Sr occupies K sites than V sites. This indicates that Sr is more likely to occupy the K site than the V site. It should be noted that the atomic radii of K, V, and Sr are 0.138, 0.058, and 0.118 nm, respectively, and K and Sr have approximately the same radii; therefore, lattice changes are minimal after replacing K with Sr, which reflects long durability of crystal structure. Along with the refinement results (Figure 1a,b; Table S2, Supporting information), upon increasing the Sr substitution level, the formation energy calculation data suggest that KS3VO has the most stable crystal structure after the substitution of Sr-ions into the K layer. We further compared the electronic and ionic conductivities of KVO and KS3VO through the density of states (DoS) and nudged elastic band (NEB) calculations (Figure 2c–g).[24] The comprehensive DoS calculation indicated a notable in the electronic conductivity of KVO upon Sr inclusion, evident in the reduction of the bandgap energy (Figure 2c,e). This is because that Sr^{2+} substitution into K^+ sites introduces charge carriers into the material, enhancing conductivity. The observed significant change in the conduction band of Sr-doped KVO than KVO with an increase in the d-orbital dominance of the vanadium atom during the charge state, as depicted in Figure 2d,f, is a noteworthy finding. This change is associated with an increase in the electron density and the facilitation of electron transport through the material's highest occupied molecular orbitals (HOMO). The dominance of d-orbitals suggests a change in the electronic structure of the vanadium atom, impacting its contribution to the conduction band. These additional energy levels are likely due to the altered electronic configuration of the vanadium atom as shown in Figure 2f. This change in electron density and the appearance of intermediate energy (presence of additional energy levels between the HOMO and the later part of the conduction band) levels contribute to the enhancement of structural overall conductivity. During the depotassiation process (charge state), this modified electronic structure allows for the free transportation of electrons throughout the material and is responsible

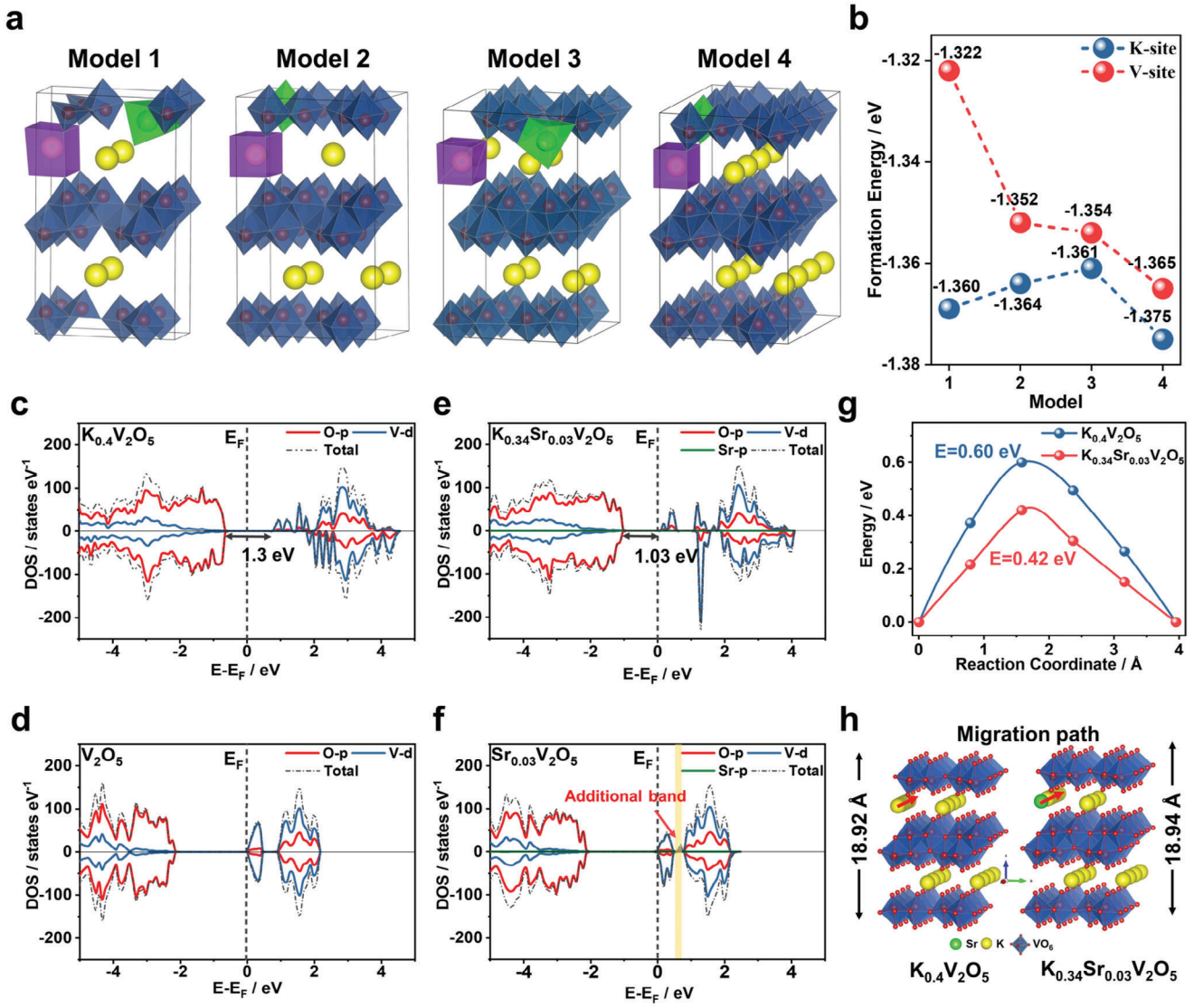

Figure 2. Panels a) illustrate K- and V-site substitution, with fluorescent and fuchsia highlighted regions indicating the presence of Sr atom and b) corresponding formation energy. Partial density of state (PDOS) of c) $K_{0.4}V_2O_5$, d) V_2O_5, e) $K_{0.34}Sr_{0.03}V_2O_5$, and f) $Sr_{0.03}V_2O_5$. Panels g,h) show the energy barrier and dedicated path of K-ion migration for $K_{0.4}V_2O_5$ and $K_{0.34}Sr_{0.03}V_2O_5$.

for higher electron mobility. The NEB calculation revealed that the predicted diffusion energy barrier of the K-ion was comparable to the previously reported K diffusion values in V_2O_5-based materials.[25,26] The NEB method combines concepts from elasticity (springs) and energy minimization to explore the potential energy surface and determine the most likely pathway for ion migration. Figure 2h illustrates the representation of the K-ion migration path within the structures. The predicted K-ion diffusion energy barrier was reduced to 0.42 eV for KS3VO (Figure 2g). DoS and NEB calculations affirm the beneficial effects of Sr substitution in enhancing the electronic conductivity and K-ion diffusion kinetics of KS3VO.

The electrochemical properties of the KVO, KS3VO, KS7VO, and KS10VO cathodes were evaluated in the voltage range of 1.5–4.2 V using coin-type cells with K metal as anode and 0.5 M potassium hexafluorophosphate (KPF_6) dissolved in a mixture of ethylene carbonate and diethyl carbonate (EC:DEC) as electrolyte. In the first charge–discharge voltage profile at 20 mA g^{-1} (**Figure** 3a,b; Figure S12c,d, Supporting information), the KS3VO and KS7VO cathodes delivered higher discharge capacities than KVO (KVO: 98 mAh g^{-1}, KS3VO: 113 mAh g^{-1}, and KS7VO: 108 mAh g^{-1}), while the KS10VO cathode showed a lower discharge capacity of 80.5 mAh g^{-1}. The introduction of K^+/vacancy induced by Sr^{2+} substitution in the K layer enhances the K^+ diffusion kinetics, leading to a significant increase in the discharge capacity of KS3VO. In particular, the KS3VO cathode exhibited lower polarization in the voltage hysteresis profile than the respective samples. Despite successful Sr substitution in the K layer, the KS7VO cathode delivered a relatively lower discharge capacity than KS3VO owing to the electrochemically inactive nature of Sr. The substantial reduction in the discharge capacity of the KS10VO cathode can be attributed to the presence of

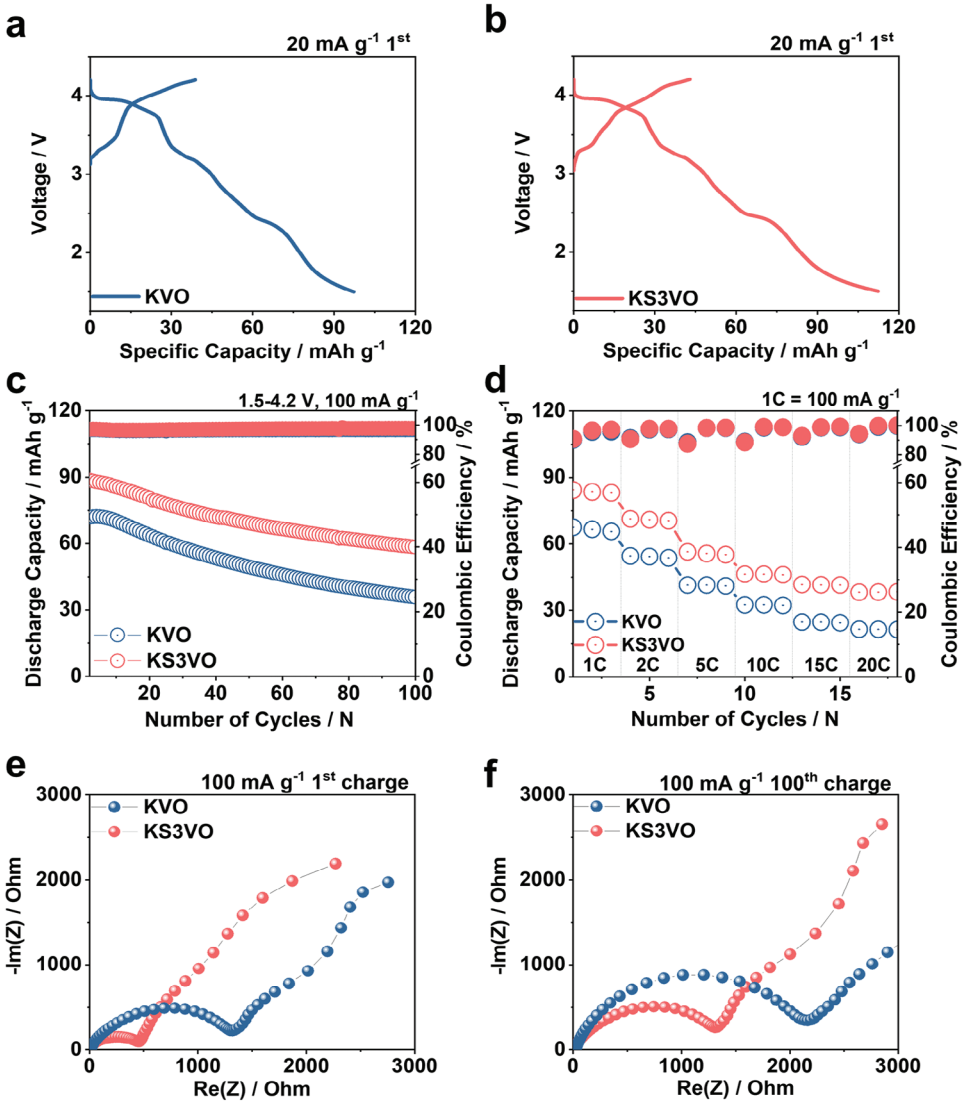

Figure 3. Electrochemical performances of $K_{0.4}V_2O_5$ (KVO) and $K_{0.34}Sr_{0.03}V_2O_5$ (KS3VO) cathodes. The charge–discharge curves of a) KVO and b) KS3VO at a current density of 20 mA g^{-1}. c) Cycling stability at a current density of 100 mA g^{-1}. d) Rate capability at various current densities from 100 mA g^{-1} to 2000 mA g^{-1} in the voltage range of 1.5–4.2 V. Nyquist plots of electrochemical impedance spectroscopy (EIS) curves of KVO and KS3VO at e) 1st cycle and f) 100th cycle.

impurities, specifically SrV_3O_{10}, in its crystal structure.[27] For the cycling test at 100 mA g^{-1}, the KS3VO cathode exhibited a higher reversible capacity and optimal cycling stability over 100 cycles (Figure 3c; Figure S12e, Supporting information). The distinctions in cycling stability between the KVO and KS3VO cathodes are directly reflected in the electrochemical impedance spectroscopy (EIS) results (Figure 3e,f). After 100 cycles, the KS3VO cathode showed more than two times smaller resistance than the KVO cathode. The K-ion diffusion coefficients (D_{K+}) for the KVO and KS3VO cathodes were subsequently calculated using the Warburg impedance data:[28,29]

$$D_{K^+} = \frac{R^2T^2}{2A^2n^4F^4C^2\sigma^2} \quad (1)$$

where R, T, A, n, F, C, and σ represent the gas constant, absolute temperature, electrode surface area, valency, Faraday constant, K-ion concentration, and the Warburg constant, respectively. For the 1st and 100th cycle, the KS3VO cathode exhibited a relatively higher D_{K+} than the KVO cathode (Table S5, Supporting information), indicating that the KS3VO cathode has better charge-transfer and ion-diffusion kinetics than the KVO cathode. The power capability of the KVO, KS3VO, KS7VO, and KS10VO cathodes was tested at various current densities ranging from 100 to 2000 mA g^{-1} (Figure 3d; Figures S12f, and S13, Supporting information). At all the current densities, the KS3VO cathode delivered the highest discharge capacity compared to other cathodes. Generally, the power capability of cathode materials in KIBs is closely linked to the electrical conductivity and diffusion kinetics of K-ions. The four-point dc method conducted at room

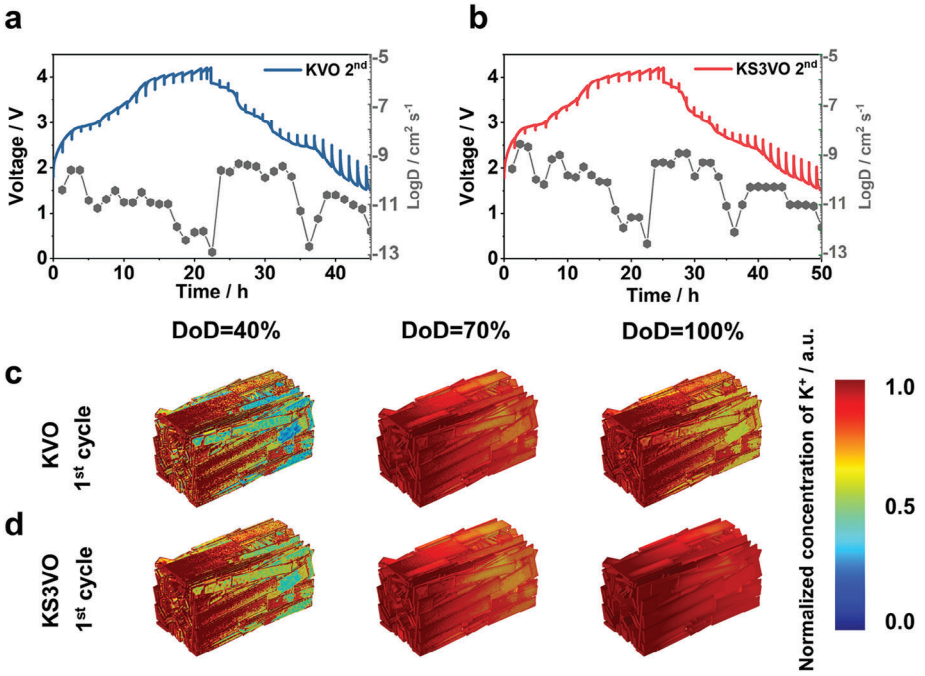

Figure 4. Galvanostatic intermittent titration technique (GITT) curves and calculated K^+ chemical diffusion coefficients for a) $K_{0.4}V_2O_5$ (KVO) and b) $K_{0.34}Sr_{0.03}V_2O_5$ (KS3VO). Potassium concentration distributions of c) KVO and d) KS3VO according to the 1st cycle degree of discharge.

temperature showed that the electrical conductivity of KS3VO (4.25×10^{-4} S cm^{-1}) is two times higher than that of KVO (1.96×10^{-4} S cm^{-1}) probably (Figure S14, Supporting information).[30,31] When Sr^{2+} ions are substituted for K^+ ions in the crystal lattice of KS3VO, it affects the electronic band structure in several ways. As shown in Figure 2f, the substitution introduced new energy levels within the bandgap, altering the mobility of charge carriers. Note that during the charge–discharge process, the layered-type cathodes experience phase transformation, which causes stress for K-ion diffusion. In addition to the D_{K+} value calculated using the Warburg impedance data, as depicted in Figure 3e,f, the galvanostatic intermittent titration technique (GITT) was further employed during the second charging and discharging process to examine the K-ion diffusion kinetics of the KVO and KS3VO cathodes. The results are illustrated in **Figure** 4a,b. Although a gradual decrease in the K-ion diffusion coefficients was observed for both KVO and KS3VO cathodes,[32] the KS3VO cathode exhibited higher K-ion diffusion coefficients than KVO during the charge–discharge process. Specifically, the average D_{K+} of the KVO cathode was $\approx 1.82 \times 10^{-10}$ cm^2 S^{-1}, while the KS3VO cathode showed a higher average D_{K+} value of 3.20×10^{-10} cm^2 S^{-1}. These results indicate that Sr substitution in the K layer improves the K-ion diffusion coefficient, leading to increased power capability. The fast charge transfer and ion diffusion kinetics of KS3VO remarkably contribute to the better K^+ storage properties of the cathode, which are further demonstrated by multi-physics simulations. The geometric models of the KVO and KS3VO cathodes used for multi-physics simulations are shown in Figure S15 (Supporting information). The spatial distribution of K-ions in different electrodes was visualized by the associated electric field, indicating the electrochemical reaction state of the cathode material. Upon the application of current density to both the KVO and KS3VO cathodes, a distinct gradient in K-ion concentration within the cathode materials became evident, extending from the surface to the bottom of the electrode. This suggests that the cathode materials near the electrode have priority to the electrochemical reaction during the discharge process. Moreover, this concentration gradient in the KVO cathode was present during the entire discharge process, from the stage of depth of discharge (DoD) = 40% to the stage of DoD = 100% after the 1st and 10th cycle (Figure 4c; Figure S16a, Supporting information). The low K-ion concentration in the KVO material at the bottom of the electrode indicates an insufficient reaction, which is consistent with the lower capacity of this material. In contrast, the K-ion concentration in the KS3VO material at the stage of DoD = 100% exhibited a remarkably uniform distribution and sufficient reaction, attributable to its faster electrochemical kinetics (Figure 4d; Figure S16b, Supporting information). These multi-physics simulation results aligned closely with the K-ion diffusion coefficients of the KVO and KS3VO from the GITT analysis data.

Cyclic voltammetry (CV) analysis was conducted to identify the electrochemical kinetic variation in K^+ storing performance between the KVO and KS3VO cathodes through their current–voltage relationship. The analyses were conducted independently at different scan rates, namely, 0.1, 0.2, 1, 2, 5, and 10 mV s^{-1} in a prescribed potential region of 1.5–4.2 V (vs K^+ /K). As the applied scan rate increased from 0.1 to 10 mV s^{-1}, similar CV patterns with broadened peaks were obtained (**Figure** 5a,b). The electrochemical diffusion (faradaic) and non-diffusion (non-Faradaic) kinetic behaviors of both cathodes were calculated and compared using the following equation:

$$i = av^b \quad (2)$$

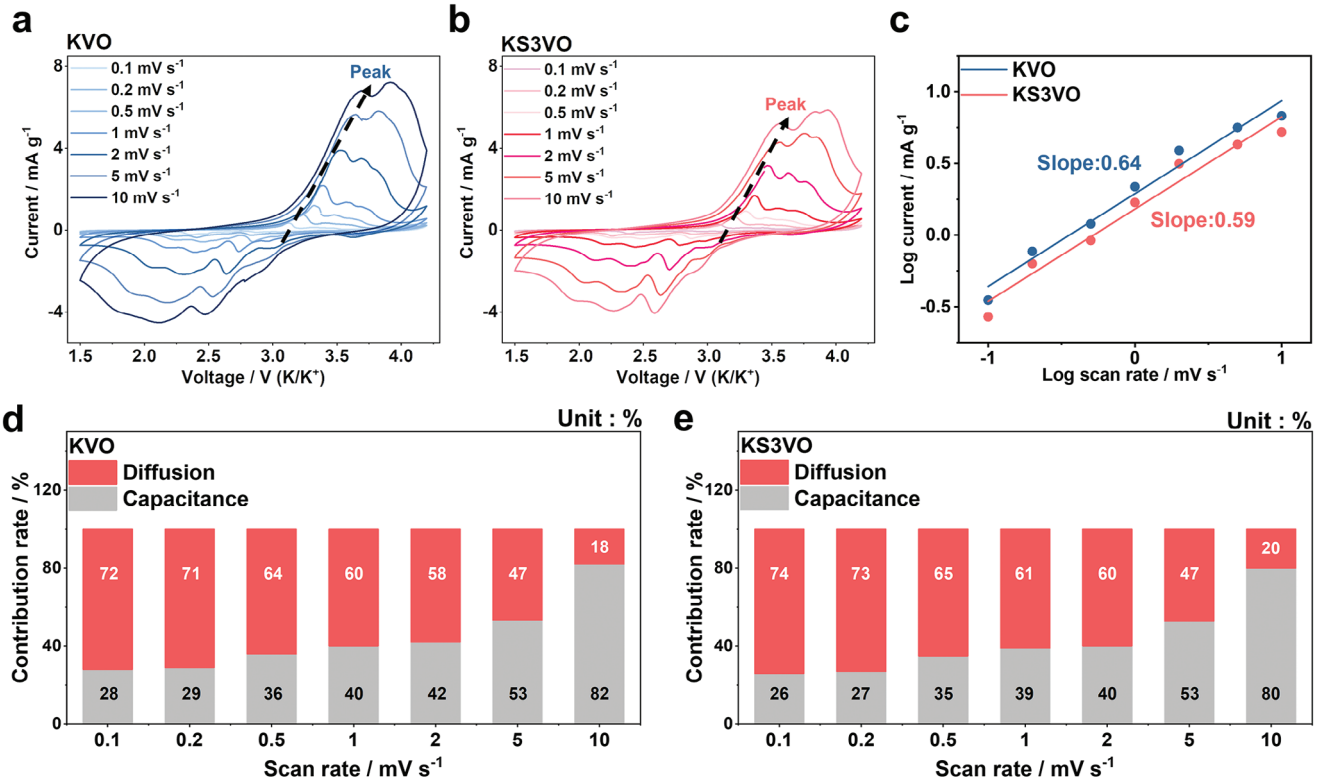

Figure 5. Cyclic voltammetry (CV) curves of a) $K_{0.4}V_2O_5$ (KVO) and b) $K_{0.34}Sr_{0.03}V_2O_5$ (KS3VO) at different scan rates from 0.1 to 1.0 mV s^{-1}. c) The plot of log (scan rate) versus log (current) was obtained from the specific peaks of the CV curves. Contribution ratio of capacitive and diffusion-controlled potassiation versus scan rate for d) KVO and e) KS3VO.

where i and v are the peak current (mA) and related scan rate (mV s^{-1}), respectively, and a and b are variables. For example, the calculated b values describe the storage process; if the value is 0.5, then it is exclusively a diffusion-controlled process; if the value is 1.0, it implies a capacitive-controlled process.[33,34] Based on the relationship between log(i)–log(v) for different redox peaks obtained during anodic and cathodic reactions, as shown in Figure 5c, the notable slope b values are 0.59 and 0.64 for KS3VO and KVO, respectively. In addition, the K^+ storage contributions of the diffusion- and capacitive-controlled processes were quantitatively estimated using the following equation:

$$i(V) = k_1 v + k_2 v^{1/2} \quad (3)$$

where the first and second parts account for the capacitive- and diffusion-controlled redox reactions, respectively. Based on this, the capacitive- and diffusion-controlled contributions were calculated for both cathodes. The diffusion and capacitive percentage contributions were calculated to be 74 and 26%, respectively, which are almost the same for KVO at the same scan rate of 0.1 mV s^{-1}. However, the percentage contribution for the capacitive control continuously increased with increasing scan rates for both cathodes and reached high values of 82 and 80%, for KVO and KS3VO at a high scan rate of 10 mV s^{-1}, respectively (Figure 5d,e). While the CV data displayed comparable controlled current and peak broadening, the KS3VO cathode exhibited smaller relative increments in current and peak broadening compared to the KVO cathode. This suggests a reduced voltage polarization achieved by stabilizing the crystal structure of KVO through Sr substitution into the K site.

The structural stability of the layered-type cathode materials greatly affects the overall cell performance during the charge and discharge reactions. To study the structural stability of the KVO and KS3VO cathodes, in situ, synchrotron X-ray diffraction (XRD) characterizations were conducted for the first two cycles in the voltage range of 1.5–4.2 V at 20 mAh g^{-1}. **Figure 6**a,b present 2D XRD contour plots with specified scanning angle (2θ) domains of 7–11° and 27–31° for KVO and KS3VO electrodes, respectively, accompanied by their voltage profiles. The 7–11° and 27–31° domains indicate the positions of the (002) and (004) peak reflections, respectively, for both samples. During the 1st charging process up to 4.0 V, KVO and KS3VO show continuous *c*-axis lattice expansion, which corresponds to a gradual shift of the (002) and (004) planes to the lower angles. After charging above 4.0 V, however, both samples undergo the *c*-axis shrinkage, which corresponds to a gradual shift of the (002) and (004) planes to the higher angles. This is because when a certain amount of K^+ is extracted from the K layer in the crystal structure results in a significant structure contraction and decreased interlayer distance. As a large amount of K^+ ions are extracted from the crystal structure, the O^{2-}–O^{2-} repulsive forces increase, resulting in structure contraction to eliminate the thermodynamical instability.[35] This behavior is generally observed for the highly charged layered-type cathode materials (high SOC

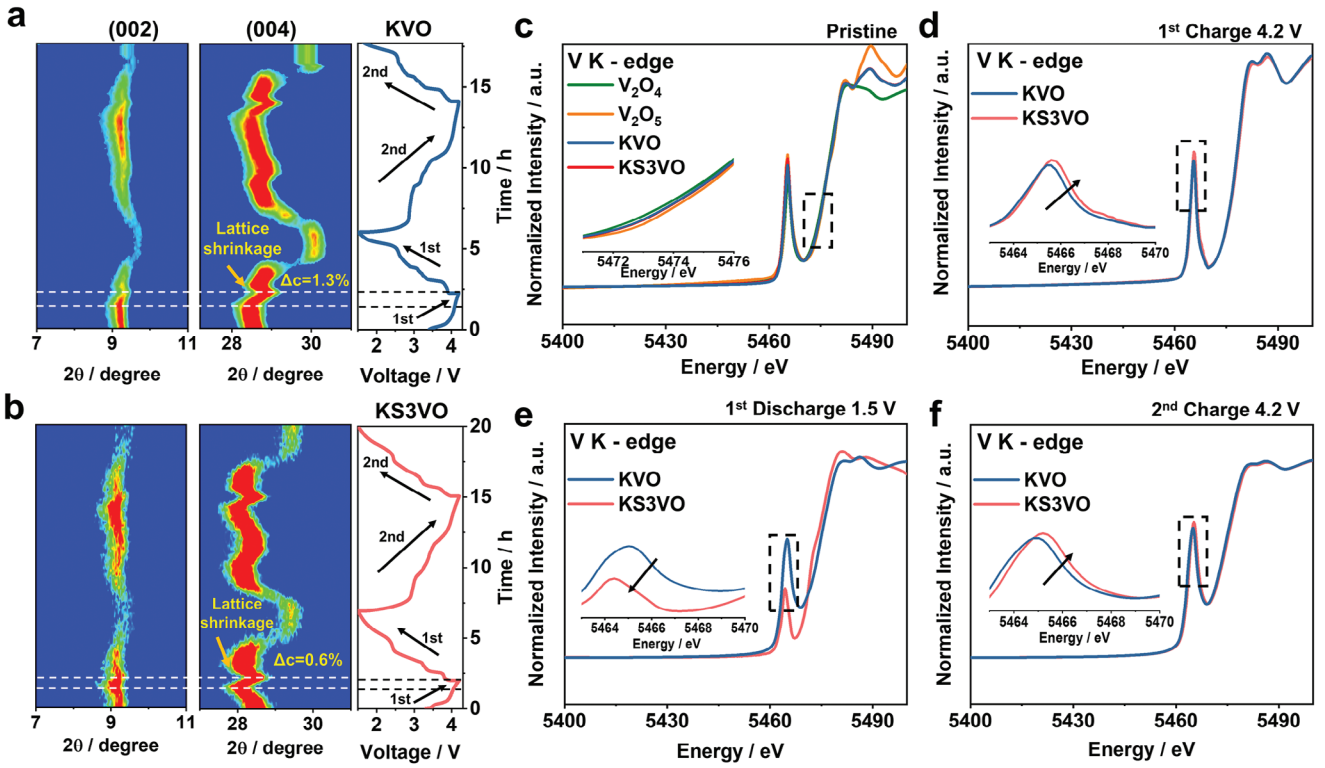

Figure 6. In-situ XRD pattern of a) $K_{0.4}V_2O_5$ (KVO) and b) $K_{0.34}Sr_{0.03}V_2O_5$ (KS3VO) during the 2nd cycles and corresponding galvanostatic charge–discharge profiles in the ranges 1.5–4.2 V. Ex situ X-ray Absorption Near Edge Structure (XANES) spectra at V-K absorption edge of KVO and KS3VO at c) Pristine state, d) 1st charged state (4.2 V), e) 1st discharged state (1.5 V), and f) 2nd charged state (4.2 V).

state) in Li and Na-ion batteries.[36–38] To further verify the lattice shrinkage of KVO and KS3VO at a high SOC state (charged at 4.2 V), we conducted a DFT calculation. The structural properties of KVO (Figure S17a, Supporting information) and KS3VO (Figure S17b, Supporting information) exhibit intriguing variations in response to changes in composition and charge state, as evidenced by the observed trends in the *c*-axis dimensions. When the K^+ extraction from the structure, an increase in the *c*-axis dimension is observed. This expansion is attributed to the increased O^{2-}–O^{2-} repulsion force. At the end of the charge (4.2 V), the structure shrinkage occurs. This tendency is consistent with the *c*-axis variation of in situ XRD data. A closer look at the (004) reflection during 2nd charge and discharge to see the *c*-axis lattice change for the KVO and KS3VO electrodes. During 2nd charging process up to 4.0 V, the change in lattice parameter c for KS3VO is lower than that of KVO (KS3VO = 5.3% vs KVO = 6.4%). From 4.0 to 4.2 V, both samples undergo shrinkage of the lattice parameter c (KVO = 1.3%, KS3VO: 0.6%).[36–38] In the highly charged state, the electrochemically inactive Sr ion acts as a pillar in the potassium layer and thus leads to a stronger Sr—O bond energy compared to the K—O bond, thereby effectively increasing the structural stability.[39,40] As the *c*-axis variation during the charge, the change in lattice parameter c for KS3VO in the discharged state is smaller than KVO (KS3VO: 4.11%, KVO: 4.39%). These results indicate the role of immobile (electrochemically inactive) Sr^{2+} as a pillar in suppressing structural stress during potassium insertion/extraction. For the (004) planes, where they are situated in the Sr and K sites, it can be observed that the expansions are suppressed due to the presence of Sr^{2+}. Furthermore, to precisely monitor the potential lattice parameter change at the charged (4.2 V) and discharged state (1.5 V), we further conducted the ex situ TEM analysis of the KVO and KS3VO. At the 2nd charged state (extraction of K^+), the interlayer distance of KVO was measured as 0.962 nm (Figure S18a, Supporting information). At the 2nd discharged state (insertion of K^+), the distance was narrower, 0.931 nm (Figure S18b, Supporting information). KS3VO showed a similar trend to KVO with slight differences in lattice parameter change after the 2nd charge and discharge process. As shown in Figure S18c (Supporting information), KS3VO shows a larger interlayer distance than the KVO. This is because the structural stability of KS3VO is more stable than that of KVO, resulting in a smaller c-axis contraction at a charged state; this trend shows in good agreement with in situ XRD data (Figure 6a,b). After the discharging process, the c-axis decreases to 0.936 nm for KS3VO (Figure S18d, Supporting information). Along with in situ XRD data, the ex situ TEM results strengthen further our conclusion that Sr substitution into KVO relieves the structural stress by reducing the lattice expansion and shrinkage rate during the charge–discharge process, eventually enhancing electrochemical performance. To enhance our understanding of the prepared cathode's reversible potassium store capability, we assessed the charged and discharged cathodes through ex situ X-ray absorption near edge structure (XANES) analysis. The V K-edges of the fresh KVO and KS3VO cathodes were compared with those of the V_2O_4 (V^{4+}) and V_2O_5 (V^{5+}) reference powders (Figure 6c). The

edge energies of the fresh KVO and KS3VO electrodes are situated between those of the V_2O_4 and V_2O_5 references, indicating that the vanadium oxidation state of the prepared sample is between V^{4+} and V^{5+}. Theoretically, vanadium exists with an average oxidation state of ≈4.8+ in the prepared samples. Figure 6d shows the V K-edge spectra of both samples after the 1st charge cycle. Notably, the pre-edge energy and intensity as well as the edge energy of the KS3VO cathode are higher than those of the KVO cathode. This indicates that more K-ions can be extracted in the KS3VO electrode, while Sr^{2+} stabilizes the structure. For the discharged KS3VO electrode (Figure 6e), the pre-edge energy and intensity as well as the edge energy of the KS3VO cathode are lower than those of the KVO cathode, suggesting that in the KS3VO cathode, vanadium exists in a lower oxidation state by storing the more K-ions in the crystal structure than that in the KVO cathode. The larger interlayer of the KS3VO cathode induced by the presence of K^+/vacancy promotes facile K-ion intercalation and results in an increased discharge capacity at the same current density. In the 2nd charged state, KS3VO showed a higher pre-edge peak change and intensity change, which corresponded to the 1st charge XANES data (Figure 6f). XANES studies confirmed the reversible vanadium redox reaction during potassium insertion/extraction and the enhanced potassium storage for the KS3VO electrode. Synchrotron-based X-ray analysis results showed that the substitution of Sr^{2+} into two K^+ sites enhanced the structural stability and electrochemical properties of the KS3VO cathode. In order to investigate the redox reaction of vanadium, X-ray photoelectron spectroscopy (XPS) analysis was further performed for KS3VO and KVO at different states of charge (Figure S19a,b, Supporting information). At the pristine state, the KVO and KS3VO cathode exhibits a similar vanadium oxidation state. For both KVO and KS3VO cathodes, the binding energy of vanadium was increased (Table S6, Supporting information) after 1st charging at 4.2 V. After following the discharging process at 1.5 V, the binding energy of vanadium shifted to a lower value for both cathodes; however, the proportion of V^{4+} in the KS3VO cathode is larger than in the KVO cathode. This trend indicated that the substitution of Sr in K layer greatly enhances the electrical and ion conductivities as well as reinforcing structural stability, leading to the reversible $V^{4+}/^{5+}$ redox reaction during the charge and discharge process.[41]

To evaluate the feasibility for practical applications, we fabricated K-ion full cells using KVO and KS3VO cathodes with hard carbon (HC) as the anode. **Figure** 7a shows a schematic of the full-cell configuration using KS3VO with the HC anode. Prior to assembling the K-ion full cells, the KVO, KS3VO cathode, and hard carbon (HC) anode were precycled in a half-cell configuration to remove the initial irreversible capacity. (Figure S20, Supporting information). A balance in the full cell was achieved by maintaining a capacity ratio of 1.2:1 between the anode and cathode (N/P ratio). The full cells were tested in the 1.5–3.9 V voltage range. In the 1st charge–discharge process at a current density of 20 mA g^{-1} (Figure 7b), the KS3VO cathode delivered a higher initial specific discharge capacity of 98 mAh g^{-1} compared to the KVO cathode (85 mAh g^{-1}). Strikingly, the KS3VO cathode demonstrated superior cycling stability with higher Coulombic efficiency and less voltage decay over 200 cycles (Figure 7c). The thermal stability of the cathode material is a critical parameter for the practical use of KIBs. The thermal stabilities of the depot-assisted KVO and KS3VO materials obtained from cathodes charged to 4.2 V (in the second cycle) were investigated using differential scanning calorimetry (DSC). Figure 7d shows the typical DSC curves from which the total specific heat generation and the temperature range at which oxygen release occurs can be determined. The thermal reaction of the KVO cathode occurs within the temperature range of 220–255 °C while that for the KS3VO occurs in the slightly higher temperature range of 230–260 °C. Specifically, the delayed onset temperature (by ≈10 °C) of the exothermic peak and the 23% reduction in the heat of enthalpy (from 284 to 218 J g^{-1}) suggest relatively slow and less oxygen evolution,[42] in deeply charged KS3VO than in its KVO counterpart. This indicates that Sr substitution enhances the structural stability and contributes to a more thermally safe KS3VO cathode in the deep charging state. In the highly charged state, the electrochemically inactive Sr ion acts as a pillar in the potassium layer and thus leads to a stronger Sr—O bond energy compared to the K—O bond, thereby effectively increasing the structural stability. Therefore, the lower quantity of oxygen evolution from the transition metal layer and thermal tolerance is due to the increased structural stability.

3. Conclusion

In this study, a novel strategy for stabilizing the layered-type KVO through Sr-substitution into the K layer was developed for the first time. The optimal amount of Sr substitution (0.03 mmol) into K sites plays two critical roles: 1) The K^+/vacancy induced by Sr-ion substitution improves the K^+ diffusion kinetics. 2) The electrochemically inactive Sr^{2+} in the potassium layer acts as a pillar, thereby suppressing the structural stress during the potassiation–depotassiation process. Compared with KVO, KS3VO demonstrated superior K^+ storage properties, with a high reversible capacity, excellent cycling stability, and power capability. In addition, the KS3VO cathode demonstrated good cycling stability in full cells using an HC anode and enhanced thermal stability. The spider map in Figure 7e shows a comprehensive summary of the overall effect of Sr substitution in stabilizing KVO explored in this work. We believe that the proposed Sr-substitution strategy will open new avenues for the stabilization of various types of layered cathode materials for high-energy KIBs.

4. Experimental Section

Computational Method: The computational simulations utilized the Vienna ab initio Simulation Package (VASP), implementing density functional theory (DFT) and adopting the projector augmented wave (PAW) method as the pseudopotential.[43–46] The generalized gradient approximation (GGA) following the Perdew–Burke–Ernzerhof (PBE) format was employed to describe the exchange-correlation interactions among the valence electrons, employing a kinetic energy cutoff of 500 eV.[47–49] To account for the strong correlation observed in the d electrons of vanadium (V), a Hubbard correction was applied with a rotationally invariant approach, as suggested by Dudarev et al., by incorporating (U–J) = 3.1 eV.[50] This choice aimed to reproduce the experimentally observed average intercalation potential of K^+. The first Brillouin zone was sampled using a 3 × 3 × 1 Γ-centered k-point mesh. Employing a Γ-centered k-point

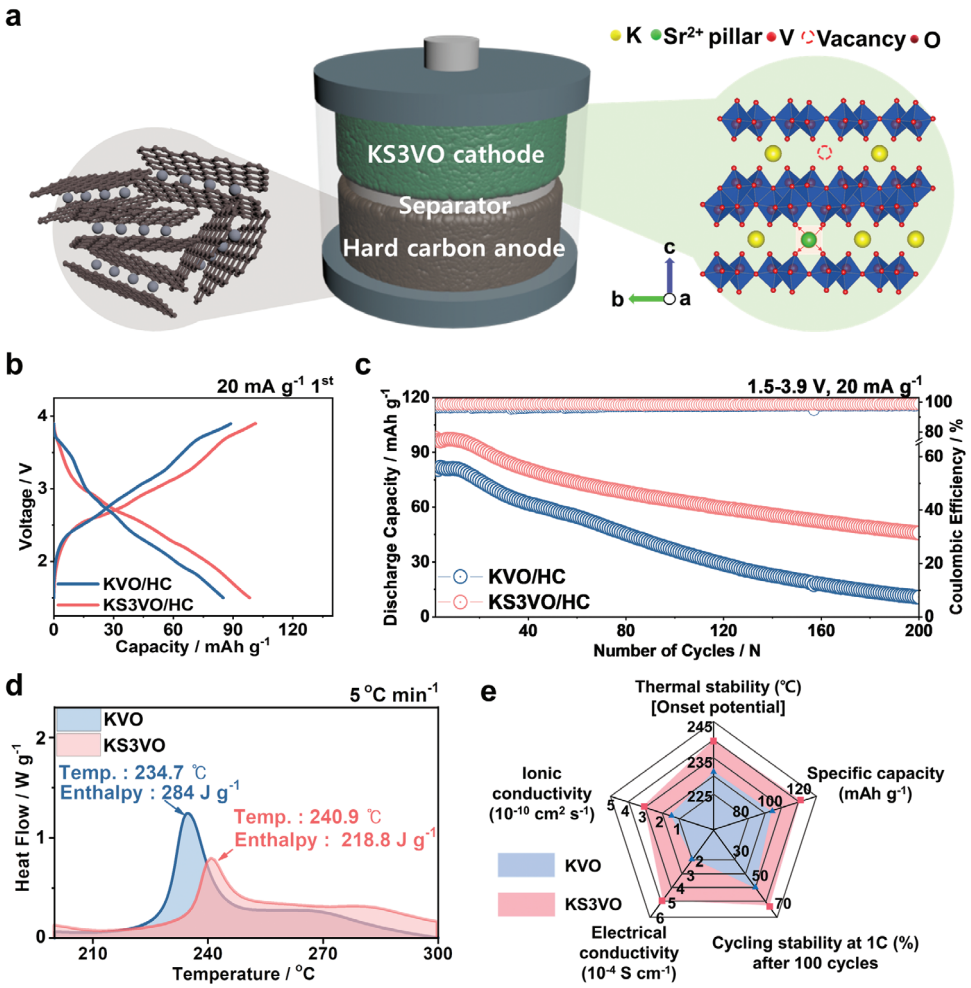

Figure 7. Electrochemical performances of the KVO/HC and KS3VO/HC full cells. a) Schematic illustration of the KS3VO/HC full cell. b) Initial charge–discharge curves of the KVO/HC and KS3VO/HC full cells at a current density of 20 mA g^{-1} in the voltage range of 1.5–3.9 V. c) Long-term cycling stability of KVO and KS3VO at a current density of 20 mA g^{-1}. d) Differential scanning calorimetry (DSC) profiles of the KVO and KS3VO electrodes. e) Comparison of the physicochemical and electrochemical characteristics of KVO and KS3VO in KIBs.

grid was a cost-effective approach that provided valuable insights into bandgaps. For smearing, the Gaussian method was used with a width of 0.05 eV and set convergence criteria at 10^{-5} eV $cell^{-1}$ for energy and 0.02 eV $Å^{-1}$ for force calculations. The DFT-D3 scheme was adopted to account for van der Waals (vdW) interactions between layers.[51] Lastly, it determined the migration barriers of K^+ through the nudged elastic band (NEB) method, applying force convergence criteria of 0.05 eV $Å^{-1}$ for each atom. There are 178 (10, 120, and 48 atoms for K, O, and V) and 236 (11, 160, 64, and 1 atom for K, O, V, and Sr) atoms in $K_{0.4}V_2O_5$ and $K_{0.34}Sr_{0.03}V_2O_5$, respectively. The lattice constants of $K_{0.4}V_2O_5$ and $K_{0.34}Sr_{0.03}V_2O_5$ are 10.97 and 11.58 Å, 18.87 Å and 14.65 Å, and 11.59 Å and 18.88 Å for a, b, and c, respectively. For the K and V site energies of Sr doped KVO, it processed $K_{0.5}Sr_{0.125}V_2O_5$ ($K_{0.5}Sr_{0.125}V_{1.937}O_5$) with 4 (4), 1 (1), 16 (15), and 40 (40) atoms of K, Sr, V, and O, respectively. Generally, when contemplating the replacement of an element within a crystal lattice, the choice of site for an atom like Sr depends on multiple factors, including ionic size, electrostatic interactions, and the imperative of sustaining charge equilibrium and minimizing perturbations to the overarching crystal structure.[52]

COMSOL Simulation: The multi-physical simulation was performed on COMSOL Multiphysics and MATLAB. The model of the cathode is built with 1 × 1 × 2 microns and the mesh size is 0.005 microns. The temperature of the electrochemical system was set at 25°. The change of dimension during the intercalation process of K-ions into the cathode was not considered. The intercalation of K-ions into electrodes was described by the classical Butler–Volmer equation[53,54]:

$$\eta_m = \Phi_s - \Phi_l - E_{eq,m} \quad (4)$$

$$i = i_0 \cdot \left(\exp\left(\frac{\alpha_a F}{RT}\eta\right) - \exp\left(\frac{\alpha_c F}{RT}\eta\right) \right) \quad (5)$$

Where η_m is the overpotential, Φ_s, and Φ_l are the electrode potential and the electrolyte potential, respectively. i_0 is the exchange current density and α is the transfer coefficient. F, R, and T are the Faraday constant, the universal gas constant, and the absolute temperature, respectively.

Synthesis of $K_{0.4-2x}Sr_xV_2O_5$ (x = 0, 0.03, 0.07, and 0.1): Orthorhombic $K_{0.4}V_2O_5$, $K_{0.34}Sr_{0.03}V_2O_5$, $K_{0.26}Sr_{0.07}V_2O_5$, and $K_{0.2}Sr_{0.1}V_2O_5$ samples were synthesized via a hydrothermal method. The precursors include potassium hydroxide (KOH, ACS regent ≥85%, pellets, Sigma Aldrich), and strontium oxide (SrO, powder, ≥99%, Sigma Aldrich). First 1 mmol of V_2O_5 (181 mg) and 0.75 mmol of KOH (42 mg) were added to 20 mL of distilled water. Following this, 0.03, 0.07, and 0.1 mmol of SrO were added and 0.2 mL of tetraethyleneglycol (TTEG) was introduced due to the reduction atmosphere during heat treatment. The solution was stirred over

2 h at room temperature, and the prepared solution was then carried to a 30 mL autoclave and heated at 180 °C for 24 h. Then, the synthesized KVO, KS3VO, KS7VO, and KS10VO were washed using D.I. water and ethanol to remove the impurities. After filtration, the mixture was oven-dried at 80 °C. To remove residual water, heat treatment was performed at 300 °C for 1 h.

Material Characterizations: The elemental compositions of the synthesized powders were determined by inductively coupled plasma (ICP) analysis using a PerkinElmer 4300 DV analyzer (Korea Basic Science Institute (KBSI). TGA characterization was conducted using a Thermo TGA, Discovery TGA500 Auto under N_2 atmosphere with a heating rate of 5 °C min^{-1}. The synthesized sample was characterized by FT-IR spectroscopy (Nicolet Is50).To confirm the oxidation state of each element from specific binding energy, it conducted XPS analysis using XPS-Theta Probe (ThermoFisher Scientific Co.). The structure and morphology of the prepared powders were identified through powder X-ray diffraction (PXRD) using a Shimadzu X-ray diffractometer with Cu Kα radiation (λ = 1.5406 Å). The Rietveld method was employed to refine the raw XRD data of all samples using GSAS-II software, and VESTA was utilized to draw the structural model derived from the refined data. Particle morphologies and sizes were determined using field-emission scanning electron microscopy (FE-SEM, HITACHI S-4700) and field emission-scanning electron microscopy (FE-TEM, Titan, FEI Corp., USA), respectively. The crystal structure and phase evolution of KVO and KS3VO were investigated through in situ X-ray diffraction using a diffractometer (Empyrean, PANalytical) equipped with a Mo Ka radiation (λ = 0.709 Å) source at a power of 60 kV–30 mA in the 2θ range of 4.6–34.5°. The cell was cycled to the charged and discharged states using a potentiostat at a current rate of 20 mA g^{-1} in the voltage range of 1.5–4.2 V (vs K^+/K). It converted the obtained in situ XRD data using Mo Kα radiation to Cu Kα radiation (λ = 1.5406 Å). Synchrotron X-ray absorption spectroscopy (XAS) was conducted at the BL7D beamline of the Pohang Light Source (PLS) using a high energy 2.5 GeV with a current of ≈200 mA to collect the ex-situ pristine, charged, and discharged states of electrodes. The collected data were converted using ATHENA software.

Electrochemical Measurements: The working electrode or cathode was prepared by blending the active material (70%), Super P (20%), and polyvinylidene fluoride (PVDF) in N-methylpyrrolidone (NMP) (10%) solvent to create a uniform slurry. This slurry was then coated with a carbon-coated aluminum foil and vacuum dried at 120 °C for 12 h to eliminate the remaining NMP and moisture. Then, this foil was pressed between stainless steel twin rollers at 120 °C for uniformity. The CR 2032-type cell was assembled, comprising a cathode and a potassium metal anode separated by a glass fiber (GB-100R). The active mass loading of the electrodes for the half-cell was 3–5 mg cm^{-2}. The electrolyte was a solution of 0.5 M KPF_6 in a mixture of ethylene carbonate/diethyl carbonate (EC:DEC) in a 1:1 volume ratio. The half-cell was stored for 2 h in a constant-temperature chamber before the electrochemical measurements. Galvanostatic electrochemical charge, discharge, and cyclic voltammetry (CV) electrochemical impedance spectroscopy (EIS) tests were conducted within a potential window of 1.5–4.2 V (vs K^+/K). These tests were carried out using a battery tester (TOSCAT) and Bio-Logic Science Instruments, respectively. For analyzing the practical point, a full-cell test was performed in the 1.5–3.9 voltage range. For the fabrication of the full cells, it used the depotassiated (charged state) KS3VO cathode and potassiated (discharged state) HC anode. The N:P ratio of the full cell was maintained at 1.2:1.

Supporting Information

Supporting Information is available from the Wiley Online Library or from the author.

Acknowledgements

G.O. and S.K. contributed equally to this work. This work was supported by the National Research Foundation of Korea (NRF) grant funded by the Korean government (MSIT) (NRF-2022R1C1C1011058) and the National Supercomputing Center with supercomputing resources including technical support (KSC-2023-CRE-0262).

Conflict of Interest

The authors declare no conflict of interest.

Data Availability Statement

The data that support the findings of this study are available from the corresponding author upon reasonable request.

Keywords

high capacity, high power, K-ion batteries, layered-type cathode, Sr substitution

Received: January 21, 2024
Revised: March 15, 2024
Published online:

[1] K. Kubota, M. Dahbi, T. Hosaka, S. Kumakura, S. Komaba, *Chem. Rec.* **2018**, *18*, 459.
[2] T. Hosaka, K. Kubota, A. S. Hameed, S. Komaba, *Chem. Rev.* **2020**, *120*, 6358.
[3] R. Zhao, H. Di, X. Hui, D. Zhao, R. Wang, C. Wang, L. Yin, *Energy Environ. Sci.* **2020**, *13*, 246.
[4] M. Zhang, J. Zhong, W. Kong, L. Wang, T. Wang, H. Fei, H. Luo, J. Zhu, J. Hu, B. Lu, *Energy Environ. Mater.* **2021**, *4*, 413.
[5] S. Komaba, T. Haseggwa, M. Dahbi, K. Kubota, *Electrochem. Commun.* **2015**, *60*, 172.
[6] Q. Zhao, J. Wang, Y. Lu, Y. Li, G. Liang, J. Chen, *Angew. Chem., Int. Ed.* **2016**, *55*, 12528.
[7] X. Wu, D. P. Leonard, X. Ji, *Chem. Mater.* **2017**, *29*, 5031.
[8] J. C. Pramudita, D. Sehrawat, D. Goonetilleke, N. Sharma, *Adv. Energy Mater.* **2017**, *7*, 1602911.
[9] Y.-S. Xu, S. Y. Duan, Y. G. Sun, D. S. Bin, X. S. Tao, D. Zhang, Y. Liu, A.-M. Cao, L.-J. Wan, *J. Mater. Chem. A* **2019**, *8*, 4334.
[10] C. Liu, Z. G. Neale, G. Cao, *Mater. Today* **2016**, *19*, 109.
[11] H. Kim, D.-H. Seo, A. Urban, J. Lee, D.-H. Kwon, S.-H. Bo, T. Shi, J. L. Papp, B. D. McCloskey, G. Ceder, *Chem. Mater.* **2018**, *30*, 6532.
[12] J.-Y. Hwang, J. Kim, T.-Y. Yu, S.-T. Myung, Y.-K. Sun, *Energy Environ. Sci.* **2018**, *11*, 2821.
[13] T. Hosaka, T. Shimamura, K. Kubota, S. Komaba, *Chem. Rec.* **2019**, *19*, 735.
[14] S. Zhao, Z. Guo, K. Yan, X. Guo, S. Wan, F. He, B. Sun, G. Wang, *Small Struct.* **2021**, *2*, 2000054.
[15] J.-Y. Hwang, S.-T. Myung, Y.-K. Sun, *Adv. Funct. Mater.* **2018**, *28*, 1802938.
[16] S. Park, S. Park, Y. Park, M. H. Alfaruqi, J.-Y. Hwang, J. Kim, *Energy Environ. Sci.* **2021**, *14*, 5864.
[17] Q. Fu, A. Sarapulova, L. Zhu, G. Melinte, A. Missyul, E. Welter, X. Luo, M. Knapp, H. Ehrenberg, S. Dsoke, *J. Energy Chem.* **2021**, *62*, 627.
[18] L. Deng, X. Niu, G. Ma, Z. Yang, L. Zeng, Y. Zhu, L. Guo, *Adv. Funct. Mater.* **2018**, *28*, 1800670.
[19] Y. Yang, Z. Liu, L. Deng, L. Tan, X. Niu, M. M. S. Sanad, L. Zeng, Z. Zhu, Y. Zhu, *Chem. Commun.* **2019**, *55*, 14988.
[20] X. Li, C. Zhuang, J. Xu, L. Li, T. Xu, S. Dai, X. Wang, X. Li, Y. Wang, *Nanoscale* **2021**, *13*, 8199.
[21] X. Niu, J. Qu, Y. Hong, L. Deng, R. Wang, M. Feng, J. Wang, L. Zeng, Q. Zhang, L. Guo, Y. Zhu, *J. Mater. Chem. A* **2021**, *9*, 13125.
[22] M. Rico, Á. E. Sepúlveda, E. Serrano, E. Lalinde, J. R Berenguer, J. G. Martínez, *J. Mater. Chem. C* **2014**, *2*, 9497.
[23] X. Niu, J. Qu, Y. Hong, L. Deng, R. Wang, M. Feng, J. Wang, L. Zeng, Q. Zhang, L. Guo, Y. Zhu, *J. Mater. Chem. A* **2021**, *9*, 13125.

[24] G. S. Gautam, P. Canepa, A. Adbellhi, A. Urban, R. Malik, G. Ceder, *Chem. Mater.* **2015**, *27*, 3733.
[25] X. Zhao, X. Zhang, D. Wu, H. Zhang, F. Ding, Z. Zhou, *J. Mater. Chem. A* **2016**, *4*, 16606.
[26] J. Carrasco, *J. Phys. Chem. C* **2014**, *118*, 19599.
[27] X. Zhang, Y. Yang, X. Qu, Z. Wei, G. Sun, K. Zheng, H. Yu, F. Du, *Adv. Funct. Mater.* **2019**, *29*, 1905679.
[28] H. Ma, X. Qi, D. Peng, Y. Chen, D. Wei, Z. Ju, Q. Zhuang, *Chem. Select* **2019**, *4*, 11488.
[29] W. Zhang, J. Ming, W. Zhao, X. Dong, M. N. Hedhill, P. M. F. J. Costa, H. N. Alshareef, *Adv. Funct. Mater.* **2019**, *29*, 1903641.
[30] G. T. K. Fey, V. Subramanian, J. G. Chen, *Mater. Lett.* **2002**, *52*, 197.
[31] Y. A. Zulueta, M. T. Nguyen, M. P. Pham-Ho, *J. Phys. Chem. Solids* **2022**, *162*, 110505.
[32] S. Fan, G. Li, F. Cai, G. Yang, *Chem. A Eur. J.* **2020**, *26*, 8579.
[33] R. Sun, S. Liu, Q. Wei, J. Sheng, S. Zhu, Q. An, L. Mai, *Small* **2017**, *13*, 1701744.
[34] H.-S. Kim, J. B. Cook, H. Lin, J. S. Ko, S. H. Tolbert, V. Ozolins, B. Dunn, *Nat. Mater.* **2017**, *16*, 454.
[35] J. Shu, R. Ma, L. Shao, M. Shui, K. Wu, M. Lao, D. Wang, N. Long, Y. Ren, *J. Power Sources* **2014**, *245*, 7.
[36] T.-Y. Yu, J. Kim, G. Oh, M. H. Alfaruqi, J.-Y. Hwang, Y.-K. Sun, *Energy Stor. Mater.* **2023**, *61*, 102908.
[37] G.-L. Xu, X. Liu, X. Zhou, C. Zhao, I. Hwang, A. Daali, Z. Yang, Y. Ren, C.-J. Sun, Z. Chen, Y. Liu, K. Amine, *Nat. Commun.* **2022**, *13*, 436.
[38] T. Li, X.-Z. Yuan, L. Zhang, D. Song, K. Shi, C. Bock, *Electrochem. Energy Rev.* **2020**, *3*, 43.
[39] I. Lee, G. Oh, S. Lee, T.-Y. Yu, M. H. Alfaruqi, V. Mathew, B. Sambandam, Y.-K. Sun, J.-Y. Hwang, J. Kim, *Energy Stor. Mater.* **2021**, *41*, 183.
[40] Y. Hou, J. Jin, C. Huo, Y. Liu, S. Deng, J. Chen, *Energy Stor. Mater.* **2023**, *56*, 87.
[41] X. Lin, X. Ren, L. Cong, Y. Liu, X. Xiang, *ChemElectroChem* **2022**, *9*, 202200669.
[42] J.-Y. Hwang, S.-M. Oh, S.-T. Myung, K. Y. Chung, I. Belharouak, Y.-K. Sun, *Nat. Commun.* **2015**, *6*, 6865.
[43] G. Kresse, J. Hafner, *Phys. Rev. B* **1993**, *47*, 558.
[44] G. Kresse, J. Hafner, *Phys. Rev. B* **1994**, *49*, 14251.
[45] G. Kreese, J. Furthmüller, *Comput. Mater. Sci.* **1996**, *6*, 15.
[46] G. Kresse, J. Furthmüller, *Phys. Rev. B* **1996**, *54*, 11169.
[47] J. P. Perdew, J. A. Chevary, S. H. Vosko, K. A. Jackson, M. R. Pederson, D. J. Singh, C. Filohals, *Phys. Rev. B* **1993**, *46*, 6671.
[48] G. Kresse, D. Jourbert, *Phys. Rev. B* **1999**, *59*, 1758.
[49] P. E. Blöchl, *Phys. Rev. B* **1994**, *50*, 17953.
[50] S. L. Dudarev, G. A. Botton, S. Y. Savrasov, C. J. Humphreys, A. P. Sutton, *Phys. Rev. B* **1998**, *57*, 1505.
[51] S. Grimme, J. Antony, S. Ehrlich, H. Krieg, *J. Chem. Phys.* **2010**, *132*, 154104.
[52] G. Perenlei, P. C. Talbot, W. N. Martens, J. Riches, J. A. Alarco, *RSC Adv.* **2017**, *7*, 15632.
[53] Y. Liu, X. Xu, O. O. Kapitanova, P. V. Endokimov, Z. Song, A. Matic, S. Xiong, *Adv. Energy Mater.* **2022**, *12*, 2103589.
[54] X. Xu, X. Jiao, O. O. Kapitanova, J. Wang, V. S. Volkov, Y. Liu, S. Xiong, *Adv. Energy Mater.* **2022**, *12*, 2200244.